EES Solar

COMMUNICATION

View Article Online
View Journal

Cite this: DOI: 10.1039/d5el00079c

Received 22nd May 2025
Accepted 3rd August 2025

DOI: 10.1039/d5el00079c

rsc.li/EESSolar

A novel way of analyzing perovskite outdoor degradation: the S-V_{oc}

Jonathan Parion,[abcd] Santhosh Ramesh,[acde] Elias Peraticos,[fg] Vasiliki Paraskeva,[fg] Matthew Norton,[fg] Maria Hadjipanayi,[fg] Tamara Merckx,[acd] Aranzazu Aguirre, *[acd] Filip Duerinckx,[acd] Hariharsudan Sivaramakrishnan Radhakrishnan,[acd] Jef Poortmans,[acde] Johan Lauwaert[b] and Bart Vermang [acd]

Perovskite mini-modules with two different electron transport layer compositions, ETL1 composed of a thick LiF/C_{60}/BCP stack and ETL2 with a thinner LiF/C_{60}/LiF stack, were located and measured outdoors for an extended period of more than three years. The analysis of the performance over time highlights a rapid degradation in the first 90 days of exposure, followed by a stabilization. Most of the initial degradation appears to be caused by a reduction in fill-factor (FF) while the open-circuit voltage (V_{oc}) remains surprisingly constant over time. The analysis of the current–voltage (IV) curves reveals that by considering these figures of merit only, the presence of important features such as S-shaped curves can be overlooked, which could lead to a wrong interpretation of the degradation origin. To address this issue, two new figures of merits, S-V_{oc} and S-FF, are introduced. The comparison between V_{oc} and S-V_{oc} shows to be an efficient and reliable way to identify S-shape formation, while enabling to quantify their contribution to performance loss. Finally, an attempt is made at understanding the origin of degradation in the perovskite mini-modules, likely an interface barrier formation in ETL1 samples and an increase in series resistance in ETL2 samples, possibly due to a partial delamination of the thinner C_{60} layer.

Broader context

Perovskite photovoltaic solar cells constitute a highly promising alternative to silicon in applications where semi-transparent, flexible or lightweight devices are required. However, their long-term stability still constitutes a critical barrier to commercialization. This work advances the field by providing a rare long-term outdoor dataset, essential for validating PSCs in real-world conditions. A key observation from the collected data is that although the V_{oc} profile seems to be constant over time for all devices, this feature is, in some cases, directly resulting from a S-shape formation and is therefore not representative of the real module performance. This is a critical issue, since previous studies on outdoor data often rely solely on these figures of merit (FoMs) for their first-level analysis. To solve this, two new FoMs are introduced here for the first time, namely S-V_{oc} and S-FF. They have the triple benefit of (a) being easy to extract even in the presence of a very large amount of IV curves (b) enabling the quantification of the S-shape formation over time and (c) constituting a closer representation of the real module. These FoMs could therefore constitute a new fast and reliable way of identifying and studying S-shapes in perovskite cells and modules.

1 Introduction

Perovskite solar cells are showing a rapid increase in technology readiness level (TRL), proving to be potentially compatible with terawatt-scale high-throughput fabrication at a reduced cost and carbon footprint.[1,2] Currently, efforts are concentrated on demonstrating the operational stability of perovskite cells and modules in the field. Although not yet standardized, many researchers use the IEC 61215 and ISOS protocols to unify and quantify reliability testing[3] and to accelerate qualification.[4]

Today, perovskite reliability testing faces three main challenges. The first is the experiment duration.[5] It is generally addressed by performing accelerated tests, but these remain time-consuming as degradation mechanisms become only evident after many hours. Furthermore, while accelerated tests can provide valuable insights, they are not adequate on their own to qualify modules for commercialization, which requires data from real-life outdoor deployment.[6–8] In this regard, the reduced number of studies exposing perovskites to outdoor conditions often reveal that these devices can degrade within a few months only. The second challenge in the field is the wide variety of perovskite material and layer stack combinations. Although degradation mechanisms for several compositions

[a]Hasselt University, Imo-imomec, Martelarenlaan 42, 3500 Hasselt, Belgium. E-mail: aranzazu.aguirre@imec.be
[b]Ghent University, Department of Electronics and Information Systems, Technology Park 126, 9052 Zwijnaarde, Belgium
[c]Imec, Imo-imomec, Thor Park 8320, 3600 Genk, Belgium
[d]EnergyVille, Imo-imomec, Thor Park 8320, 3600 Genk, Belgium
[e]KU Leuven, Department of Electrical Engineering, Kasteelpark Arenberg 10, 3001 Leuven, Belgium
[f]PV Technology Laboratory, Department of Electrical and Computer Engineering, University of Cyprus, Nicosia 1678, Cyprus
[g]PHAETHON Centre of Excellence (CoE) for Intelligent, Efficient and Sustainable Energy Solutions, Nicosia 2109, Cyprus

have already been identified,[5] they are not yet fully understood, and lack generality as well as global consensus. Finding the exact origin of the degradation therefore remains a priority.[9] The third challenge involves the reproducibility of samples. To clearly demonstrate trends in reliability studies, it is often necessary to have a relatively high number of similarly performing samples. While record stabilities are frequently reported for minimal-sized cells coated on the same substrate, some fabrication techniques still face issues with sample-to-sample repeatability.

This work aims at addressing these three challenges, by comparing the performance evolution of two device architectures over the course of more than three years. Perovskite mini-modules were manufactured with a process that is both repeatable and reproducible up to the module level[10] and placed outdoors on the island of Cyprus. The exceptionally high amount of data recovered from this analysis, over 20 000 IV curves, enables to reveal the formation of a so-called "S-shape" for ETL1 samples and to observe a large increase in series resistance for ETL2 samples. A key observation is that although the V_{oc} and FF evolution seem to be similar for both ETL compositions, the origin of their degradation is very different, as deduced from the S-shape forming in ETL1 samples only. This is a critical issue, since studies on outdoor data often solely rely on these figures of merit (FoMs) for their first-level analysis, which can therefore lead to wrong conclusions. To address this, two new FoMs are introduced in this work, namely S-V_{oc} and S-FF. By comparing these values to the extracted V_{oc} and FF, it is possible to observe the S-shape formation over time. Moreover, the absolute value of S-V_{oc} and S-FF enable to quantify the proportion of performance lost due to the S-shape. These FoMs could therefore constitute a new fast and reliable way of identifying and studying S-shapes in perovskite cells and modules. Finally, in the last part of this work, an attempt is made at identifying the cause of degradation in ETL1 and ETL2 modules. Degradation in ETL1 samples is found to be related to a barrier formation at the perovskite/electron transport layer (ETL) interface, while in ETL2 samples it is likely caused by the partial delamination of the C_{60} layer, thinner than in ETL1 samples.

2 Experimental

2.1 Device fabrication

In this study, perovskite mini-modules composed of seven monolithically series interconnected cells were made, with a total aperture area of 4 cm^2. They are arranged in a p–i–n device architecture, structured as follows: glass/ITO/hole transport layer (HTL)/perovskite/electron transport layer (ETL)/ITO. The perovskite composition selected for this research is $FA_{0.8}Cs_{0.2}Pb\ (I_{0.94}Br_{0.06})_3$. For the HTL, sputtered NiO_x is used, while the ETL is tested in two configurations: ETL1 composed of LiF/C_{60}/BCP with thickness of 0.8/40/5 nm and ETL2 composed of LiF/C_{60}/LiF with thickness of 0.8/15/0.8 nm. All test samples are laminated using a glass/glass structure of area 10 cm^2, with polyolefin (Borealis BPO8828F UV) as encapsulant material and butyl rubber (Quanex, Solargain® Edge Tape SET LP03) as edge sealant. This mini-module architecture was previously reported to demonstrate high stability under indoor accelerated testing.[11]

2.2 Measurement conditions

When placed outdoors in Cyprus, the mini-modules were arranged in a fixed plane array. IV sweeps were recorded every 15 minutes during the measurement period, first in forward and then in reverse direction. Between IV sweeps, the samples were maintained in open-circuit conditions, and occasionally placed at maximum power point (MPP), as described in previous work.[12] IV parameters were extracted from both forward and reverse IV sweeps, and an average between the two is reported for each value. For each parameter, a daily average was computed based on all the IV curve recorded at an irradiance $\geq$500 W m^{-2}. A different sweep rate was used for both ETL compositions with a value of 0.25 V s^{-1} for ETL1 samples, and 0.5 V s^{-1} for ETL2 samples. The faster scan rate was found to be less susceptible to abrupt changes in weather conditions (*e.g.*: clouds) and became the standard for measuring new modules after July 2022. While it may have impacted the samples hysteresis, it is not expected to have influenced the other figures of merit that are compared in this study, including S-V_{oc} and S-FF, as shown in the SI Fig. S1.

3 Results

3.1 Outdoor performance

Over the course of more than three years, perovskite mini-modules were installed in Nicosia, on the island of Cyprus, to study their outdoor stability in continuous operation. Two modules of each ETL composition were installed, exhibiting a similar trend in their performance evolution. This work specifically analyzes the longest performing module of each category, an ETL1 module tested between July 2021 and January 2024 and an ETL2 module tested between August 2022 and

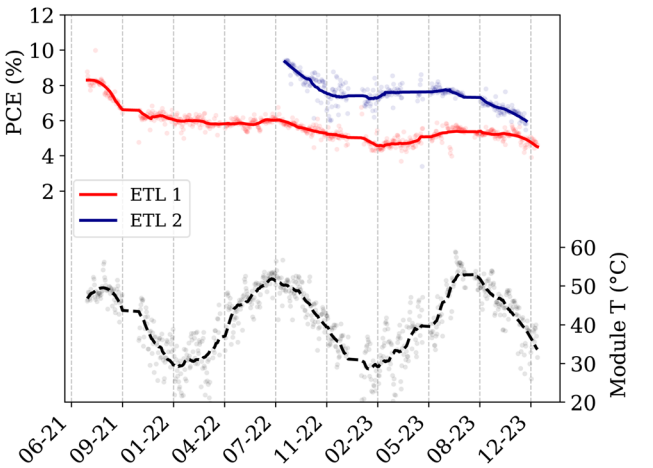

Fig. 1 Time evolution (month-year) of the mini-modules performance over a period of 3 years and 4 months, along with the modules temperature profile during the same period.

January 2024. As presented in Fig. 1, the average module temperature was comprised between 30 °C in the winter and 55 °C in the summer.

Several trends can be identified when considering the performance evolution of these mini-modules over time, as shown in Fig. 1. The daily averages are reported as measurement points, and smoothed trend lines are added for clarity in the analysis. In the initial 90 days of outdoor exposure, a rapid degradation in performance is observed. This "burn-in" period, visible in modules with both ETL compositions, is then followed by a relative stabilization of the power conversion efficiency (PCE), slightly fluctuating with seasonal changes in irradiation and temperature. During Spring (04-07/2022 and 02-07/2023), when there is a higher amount of sunshine but moderate temperatures, the performance of the module increases, while during the rest of the year the performance of the module decreases. As the most dramatic performance loss occurs during the first 90 days of outdoor exposure, the discussion section focuses on identifying the underlying mechanisms of this initial degradation.

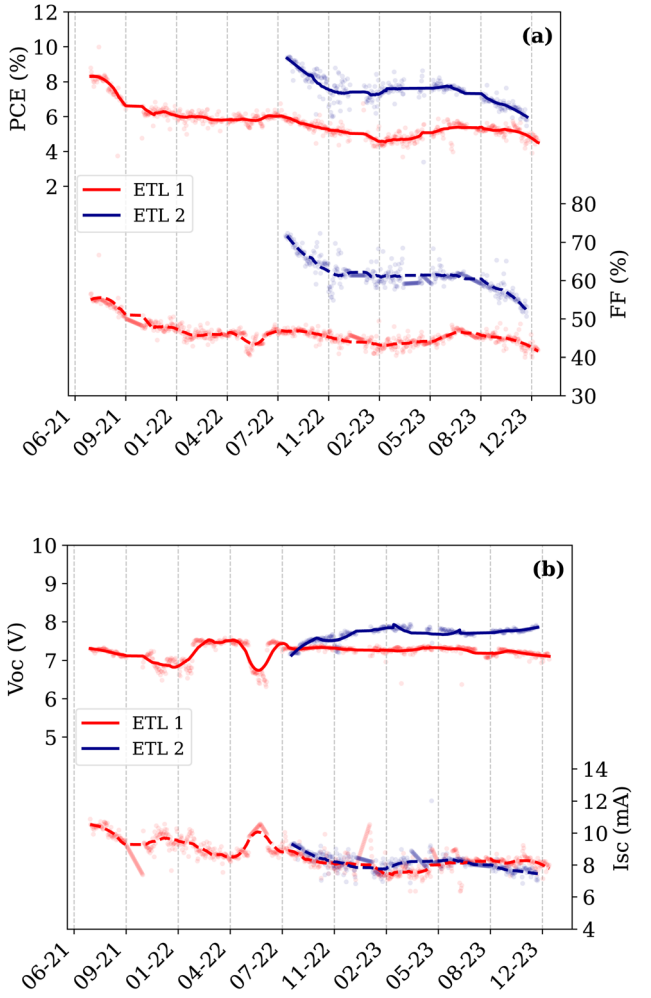

Fig. 2 (a) PCE and FF and (b) V_{oc} and I_{sc} evolution over time (month-year) for the mini-modules placed in Cyprus, reflecting the behaviour of ETL1 and ETL2 devices.

The daily averages for each of the mini-modules FoMs, along with their trend lines, are presented in Fig. 2. The open-circuit voltage (V_{oc}) appears to be relatively stable with time, showing maximum variations of 500 mV that are due to the modules either being connected to dynamic resistors for maximum power point (MPP) tracking or disconnected, therefore leaving the modules at V_{oc}. The two periods during which the ETL1 sample was placed at MPP coincide with the dips in V_{oc} and the peaks in short-circuit current (I_{sc}), visible end of 2021 and between April and July 2022. The overall variation from the start of the measurements to the final measurement days does not exceed 200 mV. Interestingly, the module with ETL2 exhibits a V_{oc} increase of approximately 500 mV during the testing period. I_{sc} deteriorates to about 70% of its initial value for both ETL1 and ETL2 devices, with a significant decline occurring within the first 90 days of exposure (Fig. 2b). The fill factor (FF) experiences total losses of approximately 30–40% over the measurement period, which significantly impacts the total performance and PCE losses. FF, I_{sc} and PCE experience an initial strong burn-in phase, resulting in around 30% losses in PCE, while an additional 10% reduction occurs over the remaining duration of the testing period. These changes are less pronounced in the ETL2 module, where the initial burn-in leads to roughly 20% losses, with the subsequent 10% decline manifesting on a longer timescale. While the overall performance evolution seem to be similar for both ETL1 and ETL2 samples, the actual degradation cause might differ. This point is addressed in the next section, aiming at providing more information on the stability behaviour of both modules, while introducing new FoMs to support their first-level analysis.

3.2 FF losses and the S-V_{oc}

To better understand the origin of the FF and V_{oc} behaviour, an extensive analysis of more than 20 000 IV curves was conducted, some of which are represented in Fig. 3. After only three months, the ETL1 module exhibits a very pronounced S-shape, contrarily to the ETL2 module which exhibits very little to no S-shape, therefore indicating a possible better tolerance to outdoor conditions. However, the sample with ETL2 still exhibit a large reduction in FF during the burn-in period, possibly related to an increased series resistance. The difference in hysteresis of the ETL2 module compared to ETL1 module is attributed to a difference in sweep rate conditions, as already mentioned in the Experimental section.

As shown in Fig. 3, the IV curves for both modules evolve in a very different way with time, the most significant difference being the S-shape appearing in the ETL1 module. This was not possible to previously deduce from Fig. 2, where the FoMs evolution seemed similar for both modules. In these circumstances, it could be questioned whether, in the presence of an S-shape, V_{oc} and FF remain effective FoMs to accurately describe the stability evolution of the perovskite modules. Indeed, only the extracted V_{oc} and FF are usually considered, therefore completely overlooking the S-shape impact in the subsequent analysis of performance. To avoid this, a new methodology is introduced to complement V_{oc} and FF with new "S-values",

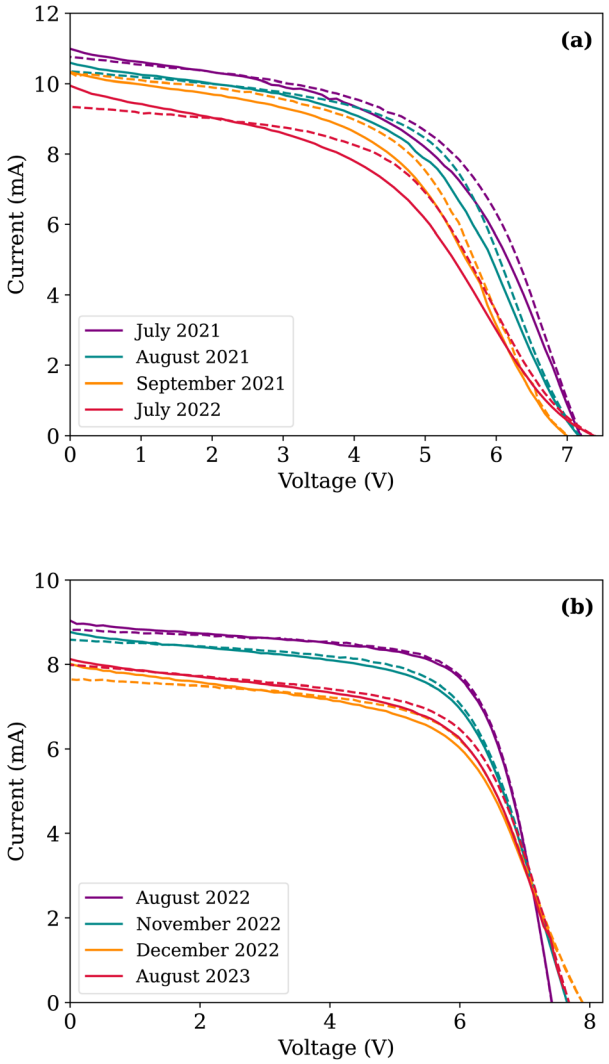

Fig. 3 Sample with (a) ETL1 and (b) ETL2 at different times of outdoor exposure. Forward sweeps are represented with a solid line while reverse sweeps are represented with a dashed line.

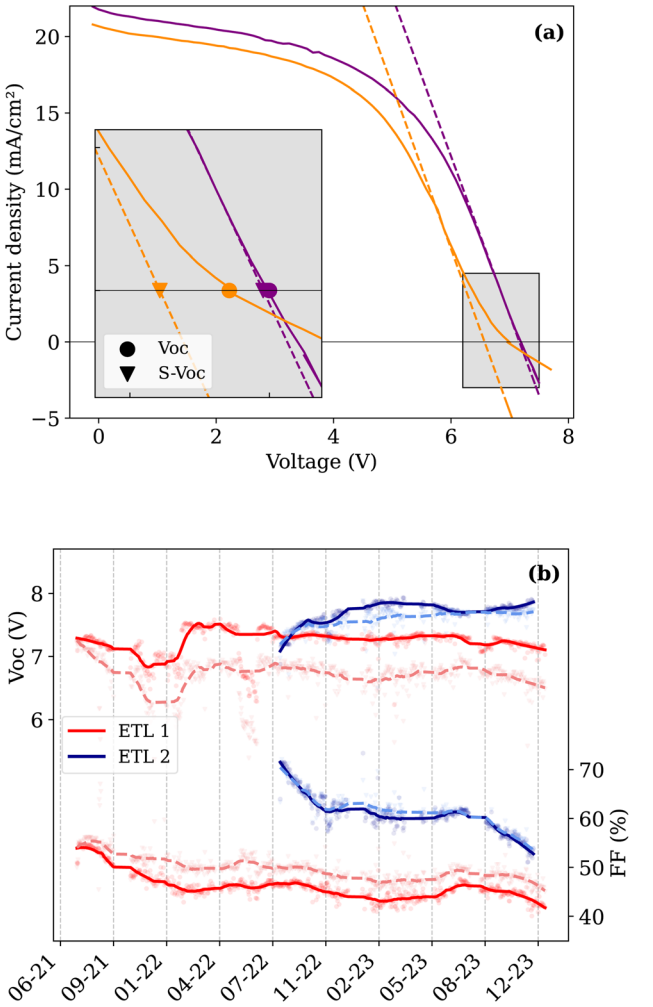

Fig. 4 (a) Methodology used to determine S-V_{oc} for quantifying the S-shape in perovskite devices. S-V_{oc} is defined as the intercept between the x-axis and the tangent to the IV curve inflexion point. When there is no S-shape, V_{oc} and S-V_{oc} overlap. (b) S-shape evolution over time for the ETL1 and ETL2 mini-modules. The measured V_{oc} and FF are represented for each module by a solid line, while the computed S-V_{oc} and associated S-FF are represented by a dashed line.

therefore enabling a quantification of the S-shape impact on IV curves FoMs. This process involves taking the tangent at the inflection point of the IV curve (Fig. 4a) and extrapolating it to find the intercept with the V-axis origin to extract a new V_{oc} value. This new value, referred to as S-V_{oc}, is lower than the real V_{oc} due to the S-shape. Based on the obtained value, FF can be re-computed to obtain the so-called S-FF as:

$$\text{S-FF} = \frac{V_{mpp} I_{mpp}}{\text{S-}V_{oc} I_{sc}}$$

with V_{mpp} and I_{mpp} being respectively the voltage and current at the device maximum power point. In Fig. 4b, the interest of these new metrics in studying the presence of S-shapes becomes very clear. In samples with little to no S-shape such as the ETL2 sample, the value of V_{oc} and S-V_{oc} stay close to each other. On the other hand, when the S-shape is more pronounced, the value of V_{oc} and S-V_{oc} strongly diverge. The same is true for FF and S-FF which are significantly different for the ETL1 sample while staying close for the ETL2 sample.

In the case of the ETL1 module, the value of V_{oc} and S-V_{oc} start diverging during the initial burn-in period of about 90 days, to eventually follow similar trends throughout the rest of the time series. During the colder months, the difference between the two values reaches its peak, while in the warmer months, this difference is at its lowest. This can be further observed in Fig. S2 (SI) where the difference between V_{oc} and S-V_{oc} is plotted against the temperature. As explained in the next section, the S-shape in ETL1 is related to the formation of a barrier at the perovskite/ETL interface. During warmer months, more thermal energy is available for charge carriers to overcome this barrier, which then explains the reduced S-shape and lower difference between V_{oc} and S-V_{oc} during that period. The "dip" in V_{oc}, which is observed in the winter of 2021, is

related to the module being placed at MPP during that period, with the dynamical load affecting the voltage reading. The same is true for May 2022, where the dip was removed from the trendline in Fig. 4b. Based on a previous study in the same climate,[12] and as well as our own indoor accelerated ageing results showing limited performance variation even when devices are exposed to 85% relative humidity (RH) for extended periods (1000 hours, in line with IEC 61215), it is not expected that relative humidity played a significant role in the seasonal dependence of S-V_{oc} and S-FF. Cyprus is known for its dry climate and the exceptionally low amount of annual precipitation. Moreover, a recent study by Remec *et al.*[13] confirms that temperature variations play a more significant role than RH in the seasonal behaviour of perovskite devices, including in more humid climates. In the case of the ETL2 module, the evolution of S-V_{oc} follows more closely the one of V_{oc} (Fig. 4b), with few or no difference between both values. This coincidence between the values of V_{oc} and S-V_{oc} can be interpreted as a significantly lower S-shape formation in ETL2 samples, which further confirms what was previously anticipated. This observation suggests that ETL2 may be better at mitigating the degradation mode leading to the S-shape, compared to its ETL1 predecessor.

In ETL1 and ETL2 modules, S-FF follows a very similar trend as S-V_{oc}. As shown in Fig. 4b, S-FF is higher than FF in ETL1, which confirms the significant impact of the S-shape on the FF. The evolution of the difference between FF and S-FF also follows a seasonal trend, where the difference is maximal during the winter months (Fig. S2, SI).

The difference in S-V_{oc} and S-FF trends between ETL1 and ETL2 samples shows that these new FoMs can provide a useful insight on the resilience of a certain stack to S-shape formation. It also constitutes a convenient tool to quantify this S-shape impact on V_{oc} and FF, while being easily applicable to large datasets such as the ones generated from outdoor data. Nevertheless, despite the usefulness of this indicator, more information is still needed as to the exact origin of the outdoor degradation in ETL1 and ETL2 modules. This point is discussed in the next section, aiming at providing further insight into the cause of degradation in perovskite mini-modules.

4 Discussion

4.1 Thermomechanical stability

The performance loss of the solar cells and modules during outdoor exposure are often attributed to the low thermomechanical stability of the stacks and encapsulation materials, which can often be compromised by extreme temperatures. Although many studies assess thermal stability by exposing samples to continuous high temperatures in dark, controlled environments, the effects of outdoor thermal and light cycling, happening in day/night cycles, are often overlooked. Long-term outdoor data, combined with indoor accelerated testing, including light/temperature cycles, aids in better understanding the primary mechanisms of degradation.

Thermal stability for this specific layer stack was previously demonstrated,[11] with experiments involving exposure to 85 °C (in nitrogen and darkness) resulting in minimal performance loss. Thermal cycling experiments consisting of 250 cycles at temperatures of −40 °C to 85 °C were moreover conducted on laminated samples, which retained 90% of their initial efficiency. Such experiments are critical, since the samples also experience daily thermal/light cycles when exposed to outdoor conditions, irreversibly impacting their stability.

The thermal expansion coefficients of the various layers in the device stack, as listed in Table 1, differ significantly between adjacent layers. This mismatch may generate strain, potentially leading to fractures. The fractures could occur in the perovskite bulk, but, although strongly dependent on perovskite composition, parameters such as fracture toughness K_{IC}, toughness G_c and hardness H_{100} are generally orders of magnitude smaller than Si, for example, from which we can conclude that the probability for internal fracture in the perovskite is lower as it is a relatively soft material.[5,14,15] Fractures are more likely to occur at the interfaces, due to a mismatch in thermal expansion coefficients. In particular, the C_{60} layer was reported to be mechanically weak and prone to easy delamination.[16–18] Often, the weakened C_{60} interface is further compromised by the sputtering damage during the processing of the subsequent layers, such as the ITO transparent electrode in the present architecture. Previous studies have identified and addressed sputtering damage after observing S-shaped IV curves.[19–21] In our case however, no S-shaped curves during IV scans performed immediately after processing were observed, which suggests that sputtering damage is either minimal or non-existent. The potential delamination of the C_{60} layer can therefore be the main reason for an increased series resistance that reflects as a decreased fill factor and short circuit current, as also previously reported in similar devices exposed to outdoor degradation.[18] This is observed especially in the ETL2 module, which is made with a thinner 15 nm C_{60} layer compared to the 40 nm C_{60} layer of their ETL1 counterpart. Nevertheless, it is also possible that this delamination and increased series resistance also occurs in ETL1 devices, hidden by the more pronounced S-shape behaviour.

4.2 Interface barrier formation

As mentioned previously, it is very unlikely that the origin of the S-shape in the IV characteristics is related to sputter damage that occurred during the deposition of the ITO contact layer,

Table 1 Thermal expansion coefficients (CTE) of the materials involved in the perovskite mini-modules, as collected from the literature

Layers stack	CTE (10–60 °C) (10^{-6} K^{-1})
Glass	3.7 (ref. 22)
ITO	8.5 (ref. 22)
NiO_x	10 (ref. 23)
FACsPbI	84 (ref. 24)
LiF	28.1–34.8 (ref. 23)
C_{60}	60 (ref. 25)
LiF	28.1–34.8
ITO	8.5
POE	36–110 (ref. 26)

since it only starts appearing as the samples begin to degrade. Furthermore, in the case of the ETL2 sample, the S-shape tends to disappear when the sample is exposed to light or elevated temperatures (Fig. 6). This would not occur if the S-shape originated from sputter damage, as that damage would likely persist. Finally, the soft sputtering process (patented[27]) used for these cells ensures minimal sputtering damage in the underlying layers, as previously demonstrated.[10]

An alternate plausible explanation is that the observed S-shape behavior is caused by the formation of an interface barrier. Typically, such a barrier can be related to either a band-alignment mismatch at one of the perovskite interfaces (injection barrier) or to a poorly conductive transport layer (extraction barrier), as explained by Tress and Inganäs.[28] By considering the normalized IV behaviour at different illumination intensities, it is possible to discriminate between these two phenomena. For this, simulations using a Devsim TCAD[29] model of the perovskite mini-module are conducted. A model with electrical parameters similar to one of the real experimental modules is constructed (SI, Table S1). To simulate the barrier, the model is first modified to include a low-mobility ETL (Fig. 5a) and is then modified again to include a barrier at the perovskite/ETL interface (Fig. 5b). The same could be done to simulate a barrier at the perovskite/HTL interface, but it is less likely to be causing issues in the experimental devices, as the NiO_x layer is more stable than the C_{60} layer. These simulated IV curves are compared to the experimental outdoor data measured for an ETL1 sample in September 2021 (Fig. 5c). As illustrated in Fig. 5a, in the presence of an extraction barrier, the normalized IV curves show significant variation at different light intensities. This is because most of the potential drops over the low mobility transport layer, effectively acting as the dielectric layer in a parallel-plate capacitor. As such, the built-in electric field in the perovskite bulk is reduced, leading to a lower photo-generated current. On the contrary, in the presence of an injection barrier (Fig. 5b), there is no screening of the potential in the perovskite bulk, leaving the photo-generated current unaffected. Only in the region close to V_{oc}, an intensity-dependent behaviour is observed, originating from the competition between the injected and generated carriers that limit the current at high illumination intensities.

A similar analysis can be conducted on outdoor experimental data by normalizing IV curves from the ETL1 sample measured at various times of the day and therefore at different irradiance levels. As shown in Fig. 5c, the normalized IV curves do not overlap, indicating a very likely extraction barrier situation. In these outdoor measurement conditions, only a limited range of illumination intensities, between 0.1 and 1 sun, are measured. However, this should be sufficient to conclude on the nature of the barrier, as clearly highlighted in Fig. 5a and b. These results were moreover also confirmed by measuring IV curves of samples with the same layer stack under a larger span of controlled irradiance levels, leading to the same observation after normalization of the IV curves. It is therefore concluded that in the ETL1 device, the apparition of an S-shaped IV curve with time is likely related to the formation of an extraction barrier at the perovskite/ETL interface.

The situation is however different in the case of the ETL2 module, which presents a much less pronounced S-shape. There, as shown in Fig. 6, the S-shape disappears after 1–2 hours of outdoor illumination only, independently of the time of year. An IV curve taken at higher irradiance level, for example around noon, does not exhibit a more pronounced S-shape similarly to what is supposed in Fig. 5. On the contrary, it seems that higher irradiance and a more elevated temperature result in a lower or no S-shape. Because of the reversible nature of the S-shape formation in the ETL2 sample, it is not possible to conclude on the nature of the interface barrier. However, this evolution of the S-shape with time gives the impression that mobile ions might be at its origin. As they go from a relaxed state in the dark and during the night to another state during the day, their motion could modify the band alignment at the perovskite/ETL interface, therefore influencing the IV curve. It is important to note that the same phenomenon could also be

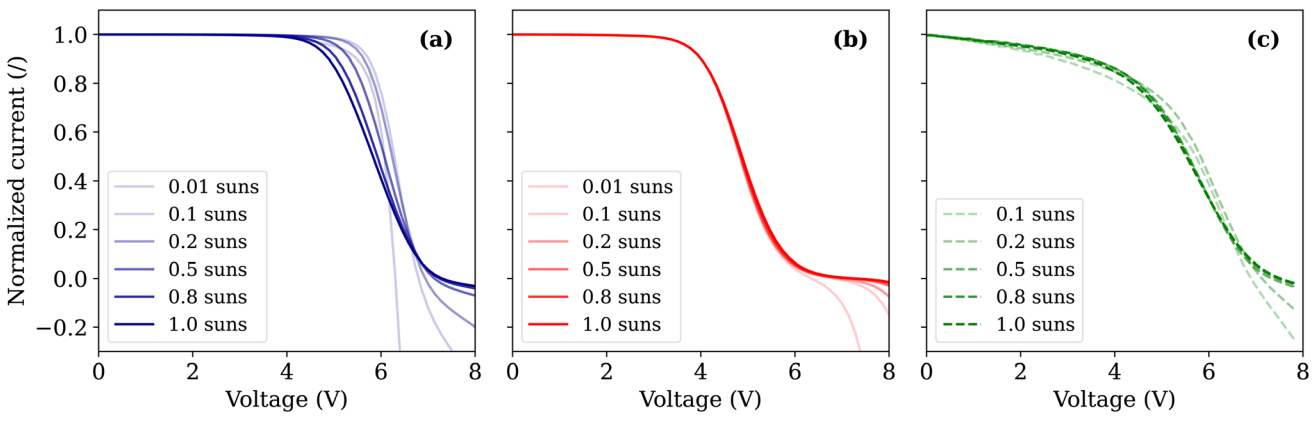

Fig. 5 Simulated and experimental IV curves of a perovskite mini-module at different illumination levels, all normalized at J_{sc}. (a) Simulated IV curve of a device presenting low ETL mobility, demonstrating the behavior of an extraction barrier, (b) simulated IV curve of a device with a band alignment mismatch between the perovskite and ETL layer demonstrating the behavior of an injection barrier and (c) experimental IV curve taken from a mini-module with ETL1, measured in Cyprus in September 2021.

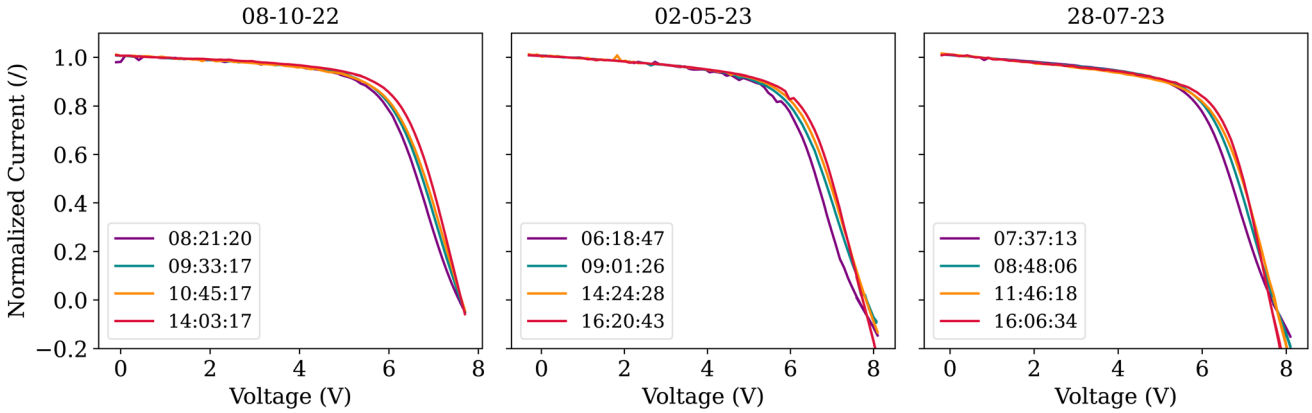

Fig. 6 Normalized IV curves taken at different dates and times for sample with ETL2. The behaviour is similar for the different timestamps, with a slight S-shape appearing in the beginning of the day when the illumination intensity is low and disappearing as the sample is exposed to light.

Table 2 Summary of the major differences in ETL1 and ETL2 modules

	ETL1	ETL2
Structure	LiF/C_{60}/BCP	LiF/C_{60}/LiF
Thickness (nm)	0.8/40/5	0.8/15/0.8
S-V_{oc}	S-$V_{oc} \neq V_{oc}$	S-$V_{oc} = V_{oc}$
S-shape	Permanent	Time-of-day dependent
FF loss	Due to S-shape	Due to R_s
Plausible origin of degradation	Extraction barrier	Partial delamination

happening in the ETL1 device, but it is not visible due to the large extraction barrier. Overall, the fact that the S-shape is less pronounced in the ETL2 module and that it even disappears after two hours of outdoor illumination demonstrates the superior capabilities and performance of ETL2 compared to ETL1, with no permanent S-shape appearing after more than 1 year of outdoor exposure.

5 Conclusion

In this work, mini-modules with two different ETL compositions were located and continuously measured outdoors for a period of more than three years. This prolonged outdoor testing enabled highlighting an initial fast decay in performance during a 90-day "burn-in" period, followed by a seasonal slight evolution of performance. A reduction in FF was found to be the main reason for the initial performance loss, while the V_{oc} either remains stable or increases over the testing period. Even though the FoMs evolution seemed similar for both ETL compositions, it appeared clearly that the origin of degradation was different, mainly because of the S-shape appearing in the ETL1 module. To enable the identification and quantification of this S-shape in perovskite solar modules, two new figures of merit, S-V_{oc} and S-FF, were introduced. They were demonstrated to be easily applicable and reliable, even on large datasets such as generated in outdoor testing. The S-shape appearing in the ETL1 device was attributed to the formation of an interface extraction barrier at the perovskite/ETL1 interface, while the increase in series resistance for the ETL2 device was attributed to the partial delamination of the C_{60} layer due to a mismatch in thermal expansion coefficients. The summary of the major differences between ETL1 and ETL2 samples is given in Table 2. Overall, this work presented a new methodology to characterize the long-term outdoor behaviour of perovskite (mini-) modules and enabled to highlight some of their main degradation pathways. This is a key step in favouring the development of high-stability, large-area perovskite solar modules.

Author contributions

Conceptualization: A. A., S. R.; data curation: J. Pa., E. P., V. P., M. N., M. H., A. A.; formal analysis: J. Pa., S. R., A. A.; funding acquisition: J. Pa., A. A., M. H.; investigation: E. P., V. P., M. N., M. H., T. M., A. A.; methodology: J. Pa., S. R., A. A.; project administration: M. H., A. A.; resources: A. A., M. H., F. D., H. S. R., J. Po., J. L., B. V.; software: J. Pa., S. R., J. L.; supervision: M. H., A. A., F. D., H. S. R., J. Po., J. L., B. V.; validation: A. A.; visualization: J. Pa., S. R., A. A.; writing – original draft: J. Pa., A. A.; writing – review & editing: all Co-authors.

Conflicts of interest

There are no conflicts to declare.

Data availability

The data supporting this article have been included as part of the SI.

Impact of sweep rate in forward curves of a perovskite mini-module similar to ETL2 module – Perovskite model parameters-Plot of (a) ΔS-V_{oc} = S-V_{oc} − V_{oc} and (b) ΔS-FF = S-FF – FF with respect to temperature and for the two different ETL compositions. See DOI: **https://doi.org/10.1039/d5el00079c**.

Acknowledgements

This work was financed by the Fonds Wetenschappelijke onderzoek (FWO) with grant number 1S01525N, by the European Union through the TESTARE project (Grant ID: 101079488) and by the European Regional Development Fund and the Republic of Cyprus through the DegradationLab project (Grant ID: INFRASTRUCTURES/1216/0043).

References

1 J. Han, K. Park, S. Tan, Y. Vaynzof, J. Xue, E. W.-G. Diau, M. G. Bawendi, J.-W. Lee and I. Jeon, *Nat. Rev. Methods Primers*, 2025, **5**, 3.
2 S. Lee, N.-G. Park and H. S. Jung, *MRS Bull.*, 2024, **49**, 1265–1274.
3 D. Zhang, D. Li, Y. Hu, A. Mei and H. Han, *Commun. Mater.*, 2022, **3**, 58.
4 M. Khenkin and S. Albrecht, *Nat. Energy*, 2024, **9**, 12–13.
5 S. Baumann, G. E. Eperon, A. Virtuani, Q. Jeangros, D. B. Kern, D. Barrit, J. Schall, W. Nie, G. Oreski, M. Khenkin, C. Ulbrich, R. Peibst, J. S. Stein and M. Köntges, *Energy Environ. Sci.*, 2024, **17**, 7566–7599.
6 Q. C. Burlingame, Y.-L. Loo and E. A. Katz, *Nat. Energy*, 2023, **8**, 1300–1302.
7 J. W. Schall, A. Glaws, N. Y. Doumon, T. J. Silverman, M. Owen-Bellini, K. Terwilliger, M. A. Uddin, P. Rana, J. J. Berry, J. Huang, L. T. Schelhas and D. B. Kern, *Sol. RRL*, 2023, **7**, 2300229.
8 H. Köbler, M. V. Khenkin, R. Roy, N. Phung, Q. Emery, M. Remec, R. Schlatmann, C. Ulbrich and A. Abate, *Energy Environ. Sci.*, 2024, **17**, 602–610.
9 N. Ahn and M. Choi, *Adv. Sci.*, 2024, **11**, 2306110.
10 M. Tutundzic, X. Zhang, S. Lammar, S. Singh, P. Marchezi, T. Merckx, A. Aguirre, E. Moons, T. Aernouts, Y. Kuang and B. Vermang, *Sol. RRL*, 2024, **8**, 2300862.
11 T. Merckx, A. Aguirre, Y. Kuang, A. van der Heide, A. Hajjiah, Y. Abdulraheem, A. Krishna, J. Poortmans and T. Aernouts, *IEEE J. Photovoltaics*, 2023, **13**, 419–421.
12 V. Paraskeva, M. Norton, A. Livera, A. Kyprianou, M. Hadjipanayi, E. Peraticos, A. Aguirre, S. Ramesh, T. Merckx, R. Ebner, T. Aernouts, A. Krishna and G. E. Georghiou, *ACS Energy Lett.*, 2024, **9**, 5081–5091.
13 M. Remec, M. Khenkin, U. Erdil, Q. Emery, G. Paramasivam, E. Unger, R. Schlatmann, S. Albrecht, M. Topič and C. Ulbrich, *Adv. Energy Mater.*, 2025, 2501906.
14 Z. Dai, M. C. Doyle, X. Liu, M. Hu, Q. Wang, C. E. Athanasiou, Y. Liu, B. W. Sheldon, H. Gao, S. F. Liu and N. P. Padture, *Scr. Mater.*, 2023, **223**, 115064.
15 Z. Dai and N. P. Padture, *Nat. Energy*, 2023, **8**, 1319–1327.
16 M. De Bastiani, G. Armaroli, R. Jalmood, L. Ferlauto, X. Li, R. Tao, G. T. Harrison, M. K. Eswaran, R. Azmi, M. Babics, A. S. Subbiah, E. Aydin, T. G. Allen, C. Combe, T. Cramer, D. Baran, U. Schwingenschlögl, G. Lubineau, D. Cavalcoli and S. De Wolf, *ACS Energy Lett.*, 2022, **7**, 827–833.
17 U. Erdil, M. Khenkin, W. M. B. de Araujo, Q. Emery, I. Lauermann, V. Paraskeva, M. Norton, S. Vediappan, D. K. Kumar, R. K. Gupta, I. Visoly-Fisher, M. Hadjipanayi, G. E. Georghiou, R. Schlatmann, A. Abate, E. A. Katz and C. Ulbrich, *Energy Technol.*, 2025, **13**, 2401280.
18 U. Erdil, M. Khenkin, W. M. Bernardes de Araujo, Q. Emery, I. Lauermann, V. Paraskeva, M. Norton, S. Vediappan, D. K. Kumar, R. K. Gupta, I. Visoly-Fisher, M. Hadjipanayi, G. E. Georghiou, R. Schlatmann, A. Abate, E. A. Katz and C. Ulbrich, *Energy Technol.*, 2025, **13**, 2401280.
19 E. Aydin, C. Altinkaya, Y. Smirnov, M. A. Yaqin, K. P. Zanoni, A. Paliwal, Y. Firdaus, T. G. Allen, T. D. Anthopoulos, H. J. Bolink, M. Morales-Masis and S. D. Wolf, *Matter*, 2021, **4**, 3549–3584.
20 T. Welzel and K. Ellmer, *J. Vac. Sci. Technol., A*, 2012, **30**, 061306.
21 J. Werner, G. Dubuis, A. Walter, P. Löper, S. J. Moon, S. Nicolay, M. Morales-Masis, S. D. Wolf, B. Niesen and C. Ballif, *Sol. Energy Mater. Sol. Cells*, 2015, **141**, 407–413.
22 J. Zhao, Y. Deng, H. Wei, X. Zheng, Z. Yu, Y. Shao, J. E. Shield and J. Huang, *Sci. Adv.*, 2017, **3**, eaao5616.
23 M. S. E. Supplies, List of Thermal Expansion Coefficients (CTE) for Natural and Engineered Materials, **https://www.msesupplies.com/pages/list-of-thermal-expansion-coefficients-cte-for-natural-and-engineered-materials**, Accessed: 2025-07-17.
24 G. Mannino, I. Deretzis, E. Smecca, A. L. Magna, A. Alberti, D. Ceratti and D. Cahen, *J. Phys. Chem. Lett.*, 2020, **11**, 2490–2496.
25 A. T. Pugachev, N. P. Churakova, N. I. Gorbenko, K. Saadli and E. S. Syrkin, *J. Exp. Theor. Phys.*, 1998, **87**, 1014–1018.
26 R. V. Dyck, T. Borgers, J. Govaerts, J. Poortmans and A. W. van Vuure, *Prog. Photovoltaics Res. Appl.*, 2021, **29**, 507–515.
27 Y. Kuang, T. Aernouts, W. Song and S. Lammar, *Method for Forming of Perovskite-Based Optoelectronic Devices*, 2024.
28 W. Tress and O. Inganäs, *Sol. Energy Mater. Sol. Cells*, 2013, **117**, 599–603.
29 J. E. Sanchez, *J. Open Source Softw.*, 2022, **7**, 3898.

